LEGIBILITY NOTICE

A major purpose of the Technical Information Center is to provide the broadest dissemination possible of information contained in DOE's Research and Development Reports to business, industry, the academic community, and federal, state and local governments.

Although a small portion of this report is not reproducible, it is being made available to expedite the availability of information on the research discussed herein.

ORNL/TM-10572
Dist. Category UC-421, 424, 426, 427

ORNL/TM--10572

DE88 010755

Fusion Energy Division

COMPACT TORSATRON REACTORS

J. F. Lyon
B. A. Carreras

V. E. Lynch
J. S. Tolliver

Computing and Telecommunications Division,
Martin Marietta Energy Systems, Inc.

I. N. Sviatoslavsky

University of Wisconsin, Madison

Date Published - May 1988

Prepared by the
OAK RIDGE NATIONAL LABORATORY
Oak Ridge, Tennessee 37831
operated by
MARTIN MARIETTA ENERGY SYSTEMS, INC.
for the
U.S. DEPARTMENT OF ENERGY
under contract DE-AC05-84OR21400

CONTENTS

ABSTRACT

Low-aspect-ratio torsatron configurations could lead to compact stellarator reactors with $R_0 = 8$–11 m, roughly one-half to one-third the size of more conventional stellarator reactor designs. Minimum-size torsatron reactors are found using various assumptions. Their size is relatively insensitive to the choice of the conductor parameters and depends mostly on geometrical constraints. The smallest size is obtained by eliminating the tritium breeding blanket under the helical winding on the inboard side and by reducing the radial depth of the superconducting coil. Engineering design issues and reactor performance are examined for three examples to illustrate the feasibility of this approach for compact reactors and for a medium-size ($R_0 \simeq 4$ m, $\bar{a} \lesssim 1$ m) copper-coil ignition experiment.

I. INTRODUCTION

It is important to find a more attractive fusion reactor concept than the conventional tokamak approach seems to allow. To be economically attractive, such a reactor should have the potential for high-beta operation, have good confinement properties, be capable of steady-state operation without large amounts of recirculating power to the plasma, and be compact to reduce unit size (and cost).

Compact reactors are particularly attractive because their smaller size allows lower total capital investment, increased mass utilization, and easier maintenance. Compact reactor size implies a low plasma aspect ratio $A_p = R_0/\bar{a}$ and coil aspect ratio $A_c = R_0/r_0$, where R_0 is the major radius of the helical field (HF) winding, r_0 is its average minor radius, and $\bar{a}$ is the average minor radius of the noncircular plasma. Sheffield's analysis[1] of generic reactor issues (beta limits, wall loading, power output, cost, etc.) points to the existence of an optimum reactor (lowest beta requirement) for $A_p \simeq 5$.

Stellarators are good candidates for such optimum reactors. Both tokamaks and stellarators obtain high plasma parameters and belong to the toroidal family of confinement devices characterized by closed, toroidally nested magnetic surfaces produced by helical (toroidal plus poloidal) magnetic fields. However, stellarators produce both toroidal and poloidal field components entirely by currents in external windings and hence do not require a net plasma current. Thus, there is no need for a continual power input to drive large toroidal currents in the plasma, as there is for an ignited, steady-state tokamak reactor. The absence of a net plasma current in stellarators eliminates the major disruptions that can terminate tokamak discharges and damage the first wall of a reactor. Since the stellarator is inherently steady state, there are no pulsed magnetic or thermal loads to accommodate, and thus it does not have the thermal and mechanical fatigue problems that dominate

tokamak reactor designs. The good confinement geometry exists without plasma, so plasma startup is on well-confined vacuum flux surfaces. Variation of currents solely in external windings allows a large degree of direct control of the magnetic configuration parameters and the flexibility to optimize the magnetic confinement geometry. Finally, the plasma temperature and density profiles in stellarators are more strongly influenced by the power and particle deposition profiles than those in tokamaks, which exhibit "self-consistent" profiles.[2] This allows more direct control of the plasma profiles that have a large influence on the overall confinement and stability of the plasma.

The torsatron is an attractive variant of the stellarator for a reactor because of its high beta potential and because both toroidal and poloidal fields are produced by unidirectional currents in external helical windings. This eliminates the need for toroidal field (TF) coils, reduces the forces on the windings, and allows extra room for reactor maintenance. (Another alternative, not discussed here, is to modularize the torsatron following the symmotron approach.[3,4])

Low-aspect-ratio torsatrons, like the Advanced Toroidal Facility (ATF) experiment[5] at Oak Ridge National Laboratory, potentially satisfy the criteria for reactor attractiveness mentioned at the beginning of this section. High volume-average beta ($\langle\beta\rangle = 5$–10%) can be obtained through direct access to the high-beta second stability region that results from beta self-stabilization and shear stabilization. Good confinement is obtained through magnetic field design and use of ambipolar electric fields to reduce cross-field direct orbit losses and diffusive losses. Steady-state operation without large amounts of recirculating power is a natural consequence of the fact that the magnetic configuration is established solely by currents in external coils.

Traditional stellarator reactor designs have high plasma aspect ratios [e.g., Heliotron H (Ref. 6) and ASRA6C (Ref. 7) with $A_p \simeq 12$ and TNPP (Ref. 8)

with A_p = 20–30] since stellarator lore has held that (equilibrium) beta limits scale as $\beta_c \propto A_p$. This scaling resulted in large values of R_0 ($\simeq$20–25 m) for the more developed Heliotron H and ASRA6C. The ATF torsatron[5] with $A_p \simeq 7$ departs from this traditional view, taking advantage of the finding[9] that, at lower A_p, direct access to a high-beta second stability region occurs. The lower-aspect-ratio ATF torsatron is a step in this direction, but further reductions in aspect ratio can be made. The studies of ATF-based reactors presented here focus on magnetic configurations that retain the high-beta potential of ATF at A_p as low as 3.5 and lead to reactors with R_0 = 8–11 m.

The low-aspect-ratio, $\ell = 2$ torsatron reactors based on the ATF configuration properties are designated Advanced Toroidal Reactors (ATRs). Three cases were selected for detailed study: ATR-1 with $M = 6$ and $A_p = 3.9$, ATR-2 with $M = 9$ and $A_p = 4.7$, and ATR-3 with $M = 12$ and $A_p = 7.8$. Here ℓ is the multipolarity and M is the number of toroidal periods of the HF winding. Obviously a range of low-aspect-ratio reactor cases exists and the optimum case could be different, but these particular cases serve to illustrate the feasibility of compact torsatron reactors. The configuration properties of low-A_p torsatrons are discussed in more detail in Ref. 10, and their scaling properties are discussed in Ref. 11.

This paper constitutes a first examination of the family of low-aspect-ratio torsatron reactors and the sensitivity of these compact reactors to various engineering and physics assumptions. Point studies of higher-aspect-ratio torsatron reactors have been carried out.[6,8] Low-aspect-ratio stellarators have also been studied by Lacatski[12] for the ATF configuration, by Hitchon[13] in generic scaling studies, and by the Kharkov group[14] in their recent Uragan-2MR study. This paper considers the implications of the more realistic configurations described in Ref. 10; the key physics issues; the consequences of engineering choices for coil, blanket, and

shielding parameters; and the projected performance for a reactor and for a small copper-coil torsatron ignition experiment.

II. LOW-ASPECT-RATIO TORSATRON CONFIGURATIONS

A family of optimized low-aspect-ratio torsatrons with properties similar to those of ATF has been described in Ref. 10. The optimization is for maximum $\iota(\bar{a})$ subject to constraints of $\iota(0) \sim 0.3$ and a central magnetic well. Here $\iota = 1/q$ is the rotational transform. These compact torsatrons have $\iota(\bar{a}) \simeq 1$ and high edge shear, and the magnetic well usually extends to the $\iota = 1/2$ surface. These properties and the resulting beta self-stabilization effect (increase of the magnetic well depth with increasing beta due to the outward Shafranov shift of the magnetic axis) result in the potential for stable, high-beta operation. In particular, the theoretically attainable beta increases with decreasing aspect ratio faster than the beta required for a given fusion power, providing more margin for reactor operation.

The $\ell = 2$ configurations are produced by either one (M odd) or two (M even) helical windings on a circular cross-section torus with a modulated winding trajectory given by $\phi = \ell[\theta - \sum \alpha_n \sin(n\theta)]/M$. Here ϕ and θ are the usual toroidal and poloidal angles, respectively, and α_n are winding modulation coefficients. The coil parameters for the three ATR cases are given in Table I, and the resulting coil geometry is shown in Fig. 1. The vertical field (VF) coils are needed to position the magnetic axis, form closed magnetic surfaces, and shape the magnetic surfaces appropriately as beta increases. Table I gives the normalized values for I, R, and Z for the VF coil sets required to create the desired magnetic configurations; B_0 is the magnetic field at $R = R_0$. Although the $M = 6$ and $M = 9$ configurations do not require an inner VF coil set, in practice all three cases would have additional VF coils to control the magnetic configuration (central rotational transform, shaping, axis shift) and to prevent net toroidal plasma currents. The optimum modulation

TABLE I.

ATR Coil Parameters

Parameter	ATR-1	ATR-2	ATR-3
M	6	9	12
α_1	0.446	0.275	0
α_2	−0.079	−0.0435	0
α_3	0.029	0	0
α_4	0.0009	0	0
$A_c = R_0/r_0$	2.50	3.24	4.49
I_{HF}/B_0R_0[a]	0.833	0.555	0.417
Outer VF coil pair			
R/R_0	1.500	1.460	1.400
Z/R_0	±0.500	±0.405	±0.305
I/B_0R_0[a]	0.275	0.213	−0.206
Inner VF coil pair			
R/R_0	—	—	0.633
Z/R_0	—	—	±0.0953
I/B_0R_0[a]	—	—	0.0625

[a] (MA·turns)·T^{-1}·m^{-1} in each coil.

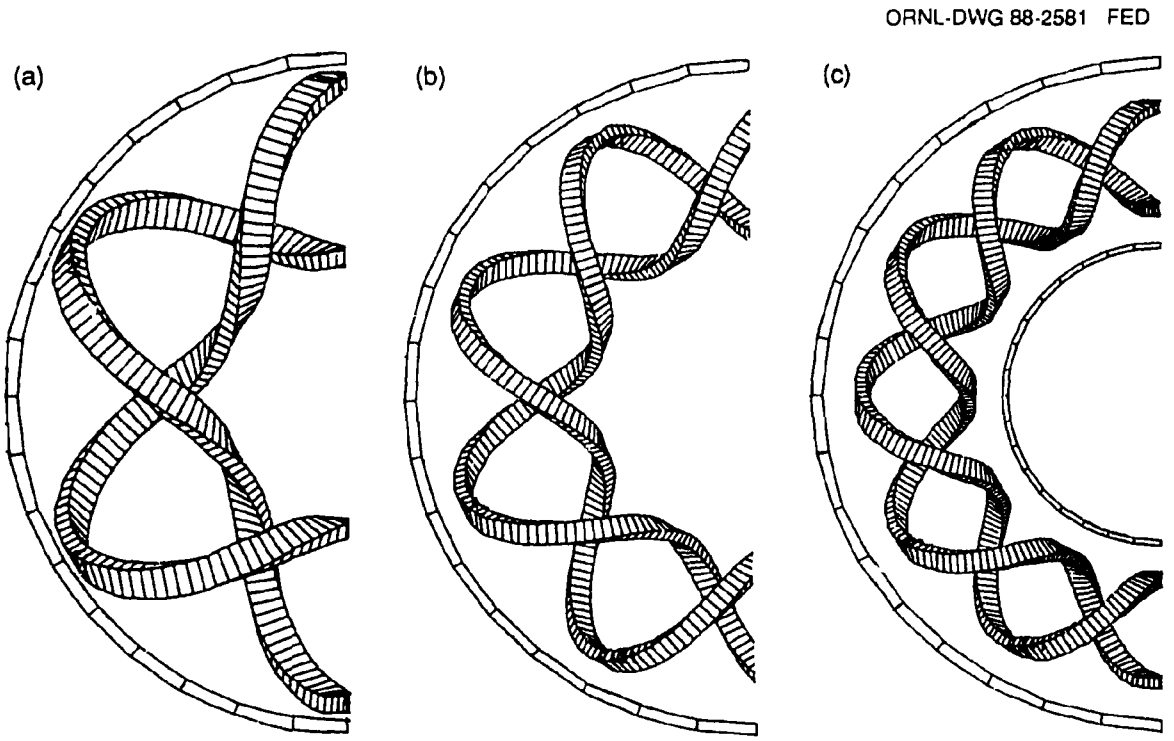

Fig. 1. Top views of coil geometry for (a) ATR-1, (b) ATR-2, and (c) ATR-3. The coil cross section is sized to give the same magnetic field on axis with the same current density in the coils.

of the HF winding and the necessary vertical field increase as M decreases. The helical coil geometry becomes more open at lower M and allows improved access for vertical removal of blanket and outer shield assemblies in a reactor.

Figure 2 shows the flux surfaces for the $M = 9$ case at different angles in a toroidal field period. The basically elliptical ($\ell = 2$) plasma cross section is distorted by toroidal effects (triangularity at $\phi = 20°$) as it rotates through a 40° field period. Although the HF windings lie on a circular cross-section torus, the last closed flux surface extends beyond this radius poloidally in the weaker field region between the windings. In contrast to a tokamak, a torsatron has a last closed flux surface (the plasma edge) because the naturally occurring separatrix breaks up into a thin ergodic region. Outside this there is a layer of diverted field lines

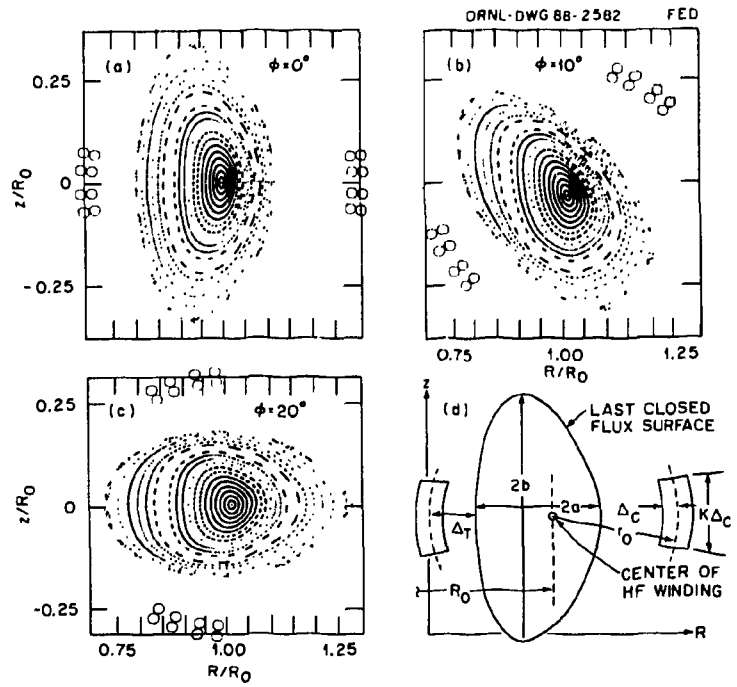

Fig. 2. The flux surfaces for the ATR-2 configuration at (a) $\phi = 0°$, (b) $\phi = 10°$, and (c) $\phi = 20°$ in a 40° field period, where the small circles show the locations of the multiple filaments used to represent the HF winding cross section in these calculations, and (d) definitions of various geometric distances used in this paper.

that can be used as a natural divertor. The diverted flux bundle is not helically symmetric at low A_p and tends to be concentrated at the outside (large R) in the equatorial plane [$\phi = (2n + 1)\pi/M$]. This feature is important both for impurity control and for control of the edge plasma density, which (as in a tokamak) is important in determining the overall transport properties (as shown in Sec. VII). These configuration features make it necessary for the first wall to have a noncircular and nonaxisymmetric cross section, but it can have a built-in divertor chamber.

Although the magnetic axis may be centered in the HF winding circle, the plasma surface is not centered. The relative outward shift of the magnetic axis with respect to the center of the last closed flux surface indicates the presence of a magnetic well, which is a feature of our optimized configurations. The radially

outward shift of the vacuum magnetic axis required to produce the vacuum magnetic well desired for magnetohydrodynamic (MHD) stability is larger at lower A_p and limits attainment of much lower A_p for reactors. As beta increases, the magnetic axis continues to shift radially outward, but the position of the outermost flux surface remains relatively unchanged. As a result, the peak neutron wall loading occurs at the outside, and the plasma boundary is closest to the coils at the inside.

The parameters that characterize the vacuum magnetic surfaces for the optimized configurations analyzed here are given in Table II. The parameter $\Delta V'/V'(0)$ is a measure of the vacuum magnetic well depth. We define $\Delta = \Delta(\theta, \phi)$ as the varying distance between the plasma edge and the center of the HF winding. The parameter Δ_m in Table II is the minimum value of Δ. It does not necessarily occur

TABLE II.

ATR Configuration Parameters

Parameter	ATR-1	ATR-2	ATR-3
M	6	9	12
$R_0/\bar{a} = A_p$	3.87	4.66	7.78
$\bar{a}/r_0$	0.646	0.695	0.577
$R/\Delta_m = A_\Delta$	6.62	8.64	9.50
$\Delta_m/\bar{a}$	0.585	0.539	0.819
Δ_m/r_0	0.378	0.375	0.473
$k = b/a$	2.10	1.81	1.69
$\iota(\bar{a})$	0.98	0.97	0.95
$\iota(0)$	0.32	0.24	0.34
$\Delta V'/V'(0)$, %	1.6	2.7	0.7

at the location shown in Fig. 2(d) and depends somewhat on the cross section assumed for the HF winding conductor. The distances Δ and hence Δ_m scale linearly with R_0 since they are properties of the magnetic configuration.

III. KEY PHYSICS ISSUES FOR LOW-$R/\bar{a}$ TORSATRONS

The usual concerns about low-A_p torsatrons are lower equilibrium beta limits and increased transport. At low A_p, beta limits are expected to be set by equilibrium limits and fragility of flux surfaces, rather than by stability limits. Concerns about lower equilibrium beta limits at lower aspect ratio are not justified for the configurations studied. The conventional wisdom states that equilibrium beta limits should scale as $\beta_c = \iota(\bar{a})^2/A_p \propto A_p$ since $\iota(\bar{a}) \propto A_p$. For low-aspect-ratio torsatrons, the symmetry-breaking effects due to $1/R$ toroidal coupling effects are significant and should lead to loss of some outer magnetic surfaces and a further reduction in the equilibrium beta limit. The torsatron configurations considered here have been optimized to restore the destroyed outer flux surfaces and have $\iota(\bar{a}) \simeq 1$, giving $\beta_c \propto 1/A_p$ instead of $\beta_c \propto A_p$.

Equilibrium beta limit calculations have been performed using the three-dimensional (3-D) VMEC and NEAR equilibrium codes for these configurations. For the pressure profiles considered, beta is limited only by equilibrium at low A_p. The outward Shafranov shift of the magnetic axis with increasing beta (stronger at lower A_p) deepens the vacuum magnetic well fast enough to overcome the destabilizing influence of the increasing plasma pressure. The finite plasma pressure can also drive currents that increase the interior shear at rational rotational transform surfaces where resonance effects are important, an effect that can be stabilizing if properly controlled with currents in external poloidal field coils. A set of inner VF coils can be effective in combating the fragility of the magnetic flux surfaces.

The concern that confinement deteriorates (in particular, that the heat diffusivity χ increases) because of the increased field ripple at low A_p is more serious. However, at low collisionality a compensating effect due to the ambipolar radial electric field can be more important than the deleterious effects of higher field ripple or finite beta distortions of the magnetic field.[15] The confinement improvement results from $\vec{E} \times \vec{B}$ poloidal orbit rotation, which reduces the usually dominant trapped particle losses arising from $\vec{B} \times \nabla B$ drifts. This mechanism applies to the thermal ions since they are in the low collisionality regime, where the heat diffusivity $\chi_i \propto \nu/E_r^2$, but not to the electrons, which are in the higher collision frequency regime where electric-field-produced rotation is not effective, so ripple trapping dominates and $\chi_e \propto \epsilon_h^{3/2}\epsilon_T^2/\nu \propto 1/A_p^2$. Here ν is the collision frequency, ϵ_h is the amplitude of the helical field ripple, and $\epsilon_T = 1/A_p$. These effects are treated in detail in Sec. VII.

Very high energy particles (in particular, the 3.5-MeV fusion-produced alpha particles) that are ripple trapped are not well confined and are not influenced by the compensating electric field effect discussed above. The loss of these particles[16] increases at lower A_p from $\simeq$15% for $M = 12$ to $\simeq$35% for $M = 6$. Fortunately, this direct alpha loss exits in a very narrow helical strip between the HF windings, and the energy can be recovered externally. The main effect of the direct alpha loss is to reduce slightly (by 15–35%) the heating power to the background plasma and hence to increase by a corresponding amount the external heating power required for ignition. A beneficial effect of this loss is the removal of the helium ash. Confined alphas slow down to energies $\sim 30\,T_e \sim 0.4$ MeV before scattering into the loss region. The bulk plasma particles with energies $\lesssim 3\,T_e \sim 40$ keV are confined by the $\vec{E} \times \vec{B}$ poloidal orbit rotation and are not affected by the high-energy loss region.

IV. MINIMUM-SIZE TORSATRON REACTORS

Two figures of merit for reactor optimization are mass utilization [kW(e)/tonne] and capital cost, both of which improve as reactor size decreases for the same power output. For the power densities considered here, the cost of electricity also decreases with reactor size. The minimum reactor size is determined by various constraints: the need to avoid spatial overlap (radial build and toroidal distance between HF windings), plasma parameter limitations ($\langle\beta\rangle$ less than some critical value), material limitations (neutron flux Γ_n at the first wall, nuclear heating power density p_d at the edge of the superconductor, and current density j versus maximum field B_{max} in the superconducting windings), and reactor requirements (power output desired, adequate space for tritium breeding, minimum cost, access for maintenance, etc.). Often these constraints are conflicting; e.g., reducing the space between the HF windings decreases the radial depth of the winding but also decreases the space available for tritium breeding. There is no unique solution. The selection depends on the weight given to the various constraints and on where compromises are made.

An important characteristic of these configurations is that the minimum distance Δ_m between the last closed magnetic surface and the center of the HF winding can be changed only by changing the size of the device. The parameter $A_\Delta = R_0/\Delta_m$ is constant for a given configuration. Because the quadrupolar helical field of the torsatron falls off rapidly with distance from the HF windings, these windings must be relatively close to the plasma surface to provide the desired level of shear in the outer region of the plasma. This is different from the case of a tokamak reactor, for which the plasma edge is defined by a material limiter or divertor coil rather than by the TF coil configuration and there is more flexibility in specifying the distance between the plasma edge and the TF coils.

For torsatron reactors, the minimum size is given by $\Delta_m = \Delta_T$, which implies $(R_0)_{\min} = A_\Delta \Delta_T$. Here we define Δ_T as the total distance needed between the plasma edge and the center of the HF winding for the plasma-wall separation, the first wall thickness, the tritium breeding blanket, the coil neutron shielding, the cryostat and coil case, and the HF winding cross section. Therefore, to minimize the size of a given magnetic configuration (A_Δ constant), we have to minimize Δ_T. The dominant terms in Δ_T come from the blanket thickness, the shield thickness required to protect the superconducting HF coil from the heating and damage associated with the intense neutron flux, and the conductor radial depth, which depends on the allowed values for current density and maximum field on the conductor. The measures taken to reduce Δ_T here are the use of a thin (tungsten rather than steel) neutron shield at locations under the HF coils where the distance to the plasma edge is small (on the small major radius side); elimination of the tritium breeding blanket at these critical locations; and a reduction in the radial depth of the HF coils (extension of the HF coil cross section in the transverse direction and higher current density).

For the Δ_T component that is independent of reactor size and field strength, labeled Δ_f, we assume 0.2 m for the plasma-wall separation, 0.01 m for the first wall thickness, zero blanket thickness where Δ is a minimum, 0.1 m for the cryostat thickness including superinsulation, 0.03 m for the coil case thickness on the plasma side (the net force is radially outward), and 0.03 m for clearance, giving a total fixed distance $\Delta_f = 0.37$ m. The shield thickness Δ_s in meters is $\Delta_s = 0.61 + 0.083 \ln(\Gamma_n/p_d)$ for steel and $\Delta_s = 0.45 + 0.058 \ln(\Gamma_n/p_d)$ for tungsten,[17] where Γ_n is the neutron wall flux in MW/m^2 and p_d is the nuclear heating power density at the edge of the superconductor in mW/cm^3. The necessary shielding thickness is 0.55 m for tungsten and 0.75 m for steel if $\Gamma_n = 5.5$ MW/m^2

and $p_d = 1$ mW/cm^3 are assumed. The value of 5.5 MW/m^2 for Γ_n is a conservative number because it includes a peaking factor of 1.7 over an average Γ_n of 3.2 MW/m^2, although the peak Γ_n occurs on the midplane at the outside, and the shield thickness constraint occurs on the midplane at the inside. This gives a constant (independent of R_0) distance $\Delta_0 = \Delta_f + \Delta_s$ of 0.92 m with tungsten shielding and 1.12 m with steel shielding. We assume a tungsten shield and no blanket under the HF winding on the small major radius side and a steel shield (with or without a thin blanket) under the HF winding on the large major radius side, where there is more room. These assumptions give a distance from plasma edge to conductor edge $\Delta_0 = 0.92$ m.

The total distance Δ_T between the plasma edge and the center of the HF winding at the closest approach point is given by $\Delta_T = \Delta_0 + \Delta_C$, where Δ_C is half the radial depth of the superconducting winding. The dependence of minimum size on the HF winding parameters enters only through Δ_C and is relatively weak, since Δ_C is usually much smaller than Δ_0 and is not a strong function of the winding parameters. For a constant current density j averaged over the conductor bundle, the value of Δ_C is given by

$$\Delta_C = \epsilon\sqrt{R_0} \tag{1}$$

where

$$\epsilon = [\pi B_0/(2\mu_0 MKj)]^{1/2} = [B_0/(8MKj)]^{1/2}. \tag{2}$$

Here B_0 is the magnetic field at the magnetic axis ($R = R_0$) in tesla, j is in kA/cm^2, and K is the aspect ratio (= transverse width/radial depth) of the HF winding cross section. Alternatively, for a given maximum field $B_{\max}$ on the conductor, the value of Δ_C is given by

$$\Delta_C = \delta R_0 \tag{3}$$

where

$$\delta = (1.32\pi B_0)/[2B_{\max}M(K+1)]. \tag{4}$$

The factor 1.32 in δ arises from calculations[16] of $B_{\max}$ using a realistic conductor cross section and the helical winding trajectory. The approximate expression for $B_{\max}$ is

$$B_{\max} = \frac{1.32\pi\sqrt{2R_0KjB_0/M}}{K+1}. \tag{5}$$

There is a weak dependence of the factor 1.32 on K and M, and in addition the results for $(R_0)_{\min}$ are relatively insensitive to these small variations.

Given Δ_C, $(R_0)_{\min}$ can be obtained from

$$(R_0)_{\min} = A_\Delta\Delta_T = A_\Delta(\Delta_0 + \Delta_C). \tag{6}$$

Using Eqs. (1) and (6) gives

$$(R_0)_{\min} = [\epsilon + (\epsilon^2 + 4\Delta_0/A_\Delta)^{1/2}]^2 A_\Delta^2/4. \tag{7}$$

Alternatively, using Eqs. (3) and (6) gives

$$(R_0)_{\min} = \frac{\Delta_0}{1/A_\Delta - \delta}. \tag{8}$$

For both Eqs. (7) and (8), no restrictions were placed on the relation between j and $B_{\max}$. However, there are stability constraints on the superconducting HF and VF windings. For Nb_3Sn internally cooled cable superconductor (ICCS), the maximum $j, B_{\max}$ pair is given[18] by $j = j_0 - 0.7B_{\max}$, where $j_0 = 13.5$ kA/cm^2, j is in kA/cm^2, and $B_{\max}$ is in tesla. It is straightforward to incorporate this constraint in the equation for $(R_0)_{\min}$. The result is

$$\Delta_C = d_1 + (d_1^2 + d_2)^{1/2}, \tag{9}$$

and hence

$$(R_0)_{\min} = A_\Delta[\Delta_0 + d_1 + (d_1^2 + d_2)^{1/2}], \tag{10}$$

where $d_1 = [0.5 + 5.8\Delta_0 K/(K+1)]/d_3$, $d_2 = \Delta_0/d_3$, and $d_3 = 8j_0 MK/(B_0 A_\Delta) - 11.6K/(K+1)$. The self-compatible values for j and B_{max} that are obtained for the minimum-size reactor are

$$j = j_0/[1 + 11.6K\Delta_C/(K+1)] \tag{11}$$

and

$$B_{max} = 16.6 j_0 K\Delta_C/(K + 1 + 11.6K\Delta_C). \tag{12}$$

The free variable in Eqs. (10)–(12) is K, the elongation of the HF winding cross section. Figure 3 shows the variation of $(R_0)_{min}$, the fraction f_B of the surface area available for breeding (i.e., that between the HF windings), B_{max}, and j. In calculating f_B, it is assumed that the blanket covers a toroidal surface whose cross section is an ellipse that rotates toroidally with the pitch of the HF windings and allows for an adequate distance between the plasma edge and the surface of the blanket. A larger value for K results in a smaller $(R_0)_{min}$ but also in less area for the tritium breeding blanket between the HF windings. In principle, the smallest

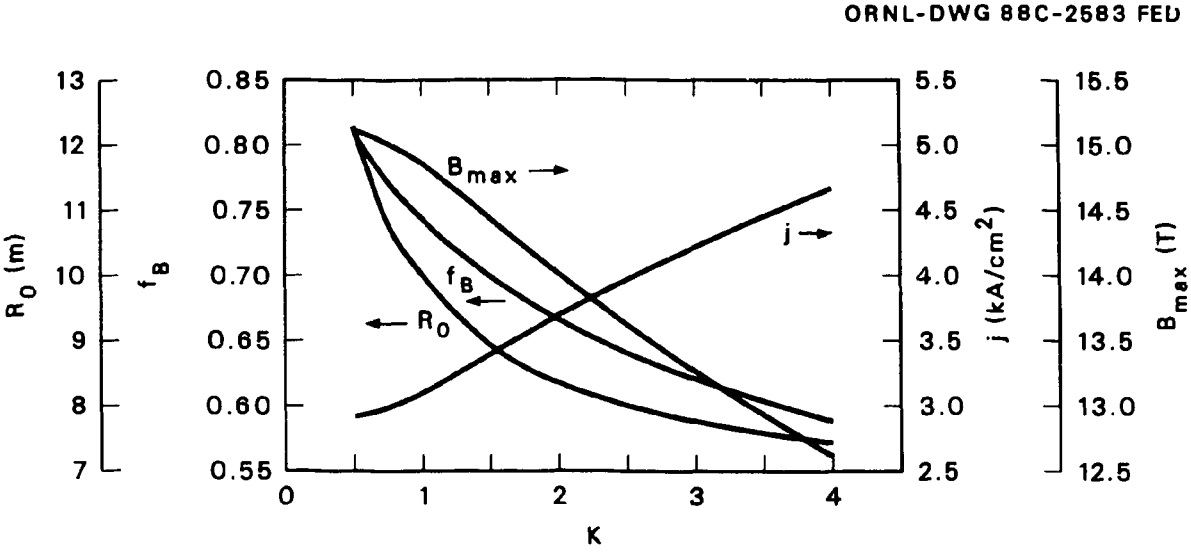

Fig. 3. Dependence of minimum-size reactor parameters on the elongation of the HF winding cross section.

value for $(R_0)_{min}$ is obtained in the extreme (but not relevant) case when $K = K_{max}$ is so large that there is no longer any space between the HF windings on the small major radius side. However, in this case, adequate space under the HF windings must be allocated for tritium breeding (and so Δ_0 is increased to 1.12 m), which severely complicates the remote maintenance issue. This results in a ridiculously high value for K (and a very thin radial depth for the HF winding), yet $(R_0)_{min}$ is larger than for modest K values when additional space (0.2 m) is allowed for the necessary blanket under the HF winding. Instead, we choose to select $K = 2$ so as to give adequate space for tritium breeding between the windings and still permit a reasonably small value for $(R_0)_{min}$. We also assume $B_0 = 5$ T for the scaling study. Equation (10) then gives $(R_0)_{min} = 8.37$ m for ATR-1, $(R_0)_{min} = 10.54$ m for ATR-2, and $(R_0)_{min} = 11.13$ m for ATR-3. These major radii are roughly one-half to one-third those of more conventional stellarator reactor designs.[6-8]

Table III illustrates the relative insensitivity of minimum reactor size to various assumptions on j, K, Δ_0, and B_0 for the $M = 6$ case. The relatively small variation in $(R_0)_{min}$ arises from Eq. (6). Case 1 is evaluated from Eq. (10) for a base set of parameters $K = 2$, $\Delta_0 = 0.92$ m, $B_0 = 5$ T, and $j_0 = 13.5$ kA/cm^2. Cases 2 through 6 differ in the value of one of these parameters, as indicated in the "comments" column of Table III. We have taken an optimistic position by assuming reliable operation with $j_0 = 13.5$ kA/cm^2 for next-century superconductors. However, reducing j_0 to 10.8 kA/cm^2 (case 2) to allow a 20% reduction in both j and B_{max} for additional margin in the superconductor only results in a 7% increase in $(R_0)_{min}$. If the less expensive steel is used for the neutron shield, then Δ_0 increases to 1.12 m (case 4) and $(R_0)_{min}$ increases by 20%. However, the cost increase in the larger reactor outweighs the saving from the cheaper shield material.[16] An increase in Δ_0 to 1.12 m would also permit a 20-cm-thick blanket under the coils on

TABLE III.

Minimum-Size $M = 6$ Reactors

Case	R_0 (m)	$\bar{a}$ (m)	j (kA/cm^2)	B_{max} (T)	Comments
1	8.37	2.16	3.69	14.02	Base case
2	8.97	2.32	2.48	11.89	$j_0 = 10.8$ kA/cm^2
3	9.36	2.42	2.80	15.28	$B_0 = 7$ T
4	10.05	2.60	3.31	14.55	$\Delta_0 = 1.12$ m
5	9.91	2.56	3.11	14.85	$K = 1$
6	7.77	2.01	4.22	13.26	$K = 3$
7	7.78	2.01	6.89	9.45	$K_{max} = 37.7$
8	5.55	1.49	4.59	12.73	Centered plasma

the small major radius side with tungsten shielding. Relatively low current density ($j = 2.5$–4.2 kA/cm^2) is a feature of all the nonextreme cases in Table III.

Larger values for $(R_0)_{min}$ are accompanied by values for $\bar{a}$ which are larger than those necessary for an attractive compact reactor. Unfortunately, it is not possible to trade some of the excess plasma radius for additional room for shielding and blankets (and hence reduced size of the reactor) since this also eliminates the outer part of the rotational transform profile and thus affects the MHD properties of the magnetic configuration. Modular stellarators with their relatively flat $\iota(r)$ profiles and tokamaks do not have this constraint. Similarly, it is not possible to "center" the flux surfaces in the coil bore since this eliminates the vacuum magnetic well upon which the favorable MHD properties depend. However, even if this were

possible, it would not help, since the value of Δ halfway through a field period where the long axis of the plasma is horizontal is not much larger than Δ_m. Simple geometric models that overlook the fact that the plasma is not centered with respect to the helical coils, especially at low aspect ratio, and ignore the winding law modulation typically underestimate the plasma aspect ratio and the minimum attainable reactor size by ~30%. This is because the effective but unrealistic Δ_m is significantly larger for the plasma edge centered in the HF winding circle. Thus, $A_\Delta = 4.74$ and $(R_0)_{\min} = 5.55$ m for case 8 versus $A_\Delta = 6.32$ and $(R_0)_{\min} = 8.37$ m for case 1.

V. REACTOR TORUS COMPONENTS

The principal components of the reactor torus (other than the vacuum vessel) are the coil shielding, the superconducting HF coil, and the tritium breeding blanket. The largest of these is the coil shielding. The tungsten shield thickness of 0.55 m and the steel shield thickness of 0.75 m were obtained for 1 mW/cm^3 of nuclear heating at the surface of the superconductor, chosen so that the cryoplant capacity needed to compensate for nuclear heating in the coils is 2% of the net electrical output. Our assumption gives 3×10^{10} rad of exposure to the insulators after 30 full-power years, and the magnet would be annealed every 8 full-power years. Increasing the shielding thickness (by 0.13 m with tungsten or 0.19 m with steel) reduces p_d to 0.1 mW/cm^3, the insulator exposure to 3×10^9 rad, and the cryoplant capacity to 0.2% of the electrical output, and the magnet does not have to be annealed. We choose the less conservative values. The thickness of the shielding on the sides of the HF winding is taken to be 45% of the thickness of the shielding facing the plasma to account for the grazing incidence of the neutron flux on the sides of the HF winding. A reasonable radiation limit for electrical insulation (Spalrad-S polyimide) is 10^{11} rad, and there is no practical limit for thermal insulation (aluminum foil with glass paper). For

the superconducting coils, a radiation limit of 4×10^{19} n/cm^2 is assumed for the Nb_3Sn conductor, and there is no practical limit for the copper stabilizer since it is cryostable with an increase in resistivity of 0.3 $\mu\Omega$·cm.

Table IV gives the device parameters for ATR-1, ATR-2, and ATR-3, all with $B_0 = 5$ T and 4-GW fusion power. The increment in the total thermal power over the 4-GW fusion power is due to the energy multiplication in the blanket structure. The weights given in Table IV are for ATRs with blankets under the outboard part of the HF windings. If this blanket is omitted, the main blanket thickness increases to compensate for the reduced breeding area, the total weight drops by $\simeq$5%, the total thermal power drops by $\simeq$7%, and the mass utilization drops by 2.4% for ATR-1 and ATR-2. The total weight of these reactors varies between 8,200 and 11,040 tonnes. The mass utilization efficiency varies between 170 and 230 kW(e)/tonne; the usual goal for an attractive reactor is $\geq$100 kW(e)/tonne.

An important issue for these reactors is adequate space for tritium breeding with an acceptable breeding ratio. Table IV shows that the fraction of the torus surface available for tritium breeding is 76% for ATR-1 and 72% for ATR-2 with a thin blanket under the outboard 41% of the HF winding versus 60% and 56% without the blanket. The tungsten shield covers the inboard 45% of the HF winding and the iron shield covers the outboard 55%. Tritium breeding is possible over $\simeq$75% of the length of the iron shield under the HF winding. The required net tritium breeding ratio is 1.05, so the local tritium breeding ratio must be 1.38 and 1.45 with a blanket under the outboard part of the HF windings versus 1.75 and 1.88 with no blanket under the HF windings for ATR-1 and ATR-2. Either situation is acceptable; the decision is between the inconvenience of the required access to the blanket under the outboard part of the HF winding versus the need for a higher tritium breeding ratio without that blanket segment. There is no choice for the

TABLE IV.

Engineering Parameters for ATR Cases

Parameter	ATR-1	ATR-2	ATR-3
Size			
Major radius (m)	8.37	10.54	11.13
Minor coil radius (m)	3.34	3.25	2.47
Plasma radius (m)	2.16	2.26	1.43
Helical coils			
Current (MA · turns)	34.89	29.27	23.18
Cross section (m × m)	0.69×1.38	0.60×1.20	0.50×1.01
Coil length (m)	158.2	223.3	233.7
Maximum radial body force (MN/m)	82.6	59.6	51.1
Front shield thickness (m), W	0.55	0.54	0.56
Front shield thickness (m), Fe	0.75	0.74	0.77
Blanket			
Area available for breeding (%)	60.0	56.0	45.0
Required breeding ratio	1.75	1.88	2.33
Breeding required under coils?	No	No	Yes
Blanket thickness (m)	0.29	0.34	–
Local blanket energy multiplier	1.56	1.53	–
Area available (if breed under coils) (%)	76.0	72.0	67.0
Required breeding ratio	1.38	1.45	1.57
Blanket thickness (m)	0.18	0.21	0.23
Local blanket energy multiplier	1.59	1.58	1.57
Weights (tonnes) with breeding under coils			
Helical coil + case	1514	1597	1153
W coil shield	1378	1738	1660
Fe coil shield	325	419	446
Blanket	403	547	392
Reflector	2342	2643	1563
Shield	690	777	441
VF coils + case	299	363	434
Vacuum vessel	2435	2955	2112
Total weight	9386	11039	8201
Power			
Fusion power (MW)	4000	4000	4000
First wall area (m^2)	947	1190	816
Neutron wall load (MW/m^2)	3.38	2.69	3.92
Total thermal power (MW)	5371	5270	5220
Net electrical power (MW), $\eta = 0.36$	1934	1897	1879
Mass utilization [kW(e)/tonne]	206	172	228

ATR-3 case; the small fractional area (45%) for breeding and the high breeding ratio required (2.33) without the outboard blanket make that blanket segment necessary.

Figure 4 illustrates the proposed blanket structure.[19] It is 25 cm thick and made of HT-9 ferritic steel with close-packed beryllium balls as the neutron multiplier and moderator and $Li_{17}Pb_{83}$ in the voids as the breeding material. The

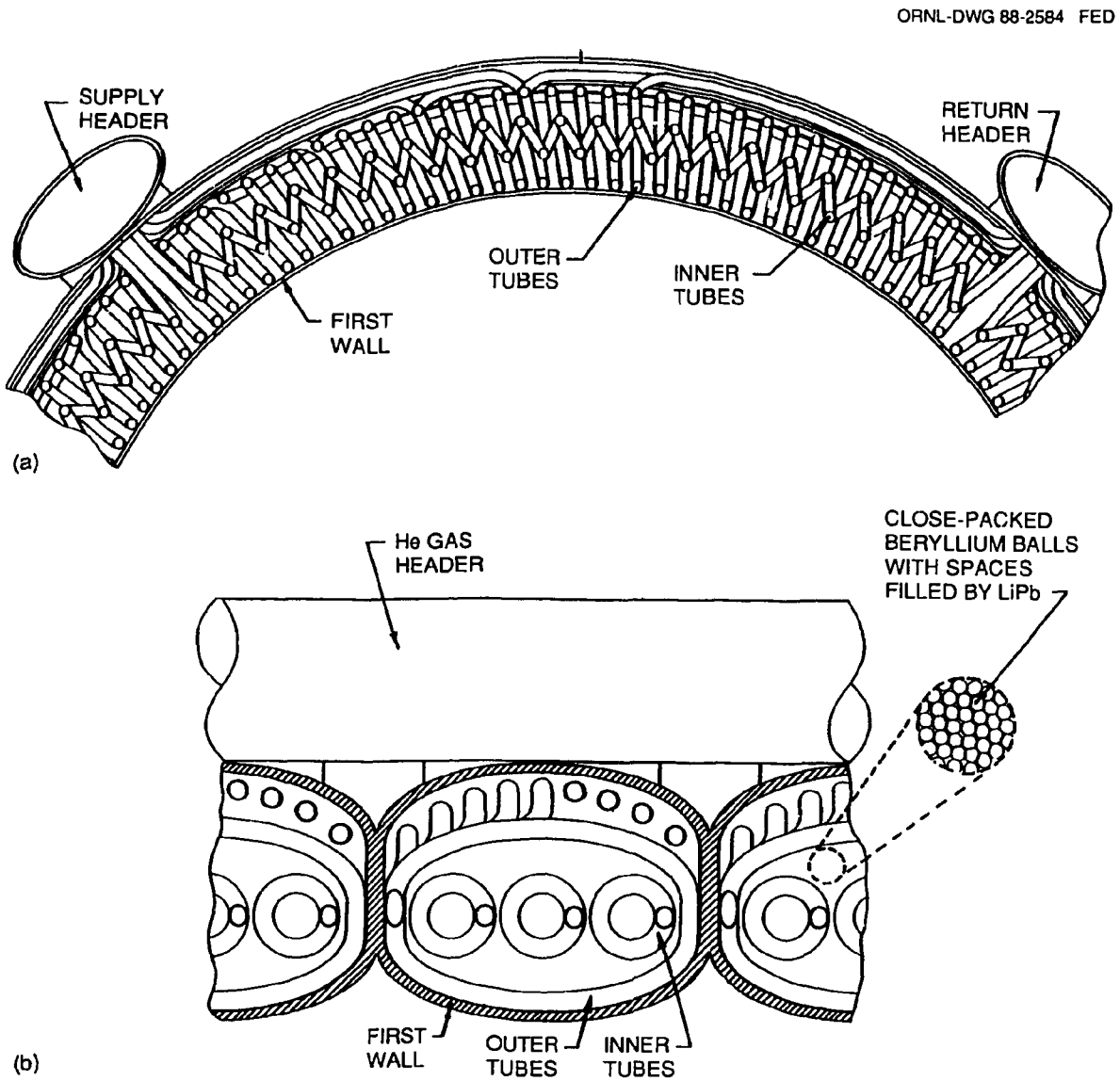

Fig. 4. Proposed thin tritium breeding blanket structure for ATRs. (a) Cross section at a constant toroidal angle. (b) Cross section at a constant poloidal angle.

volume percentages are 70% beryllium, 10% $Li_{17}Pb_{83}$, 10% HT-9, and 10% helium. The high beryllium fraction is obtained from the variation of tritium breeding ratio and neutron multiplication factor versus volume percentage of beryllium shown in Fig. 5. The material fractions were optimized for a 40-cm-thick blanket, but our experience has shown that these fractions are also optimum for blanket thicknesses down to 15 cm. The breeding ratio and multiplication factor for a blanket of this composition are shown versus blanket thickness in Fig. 6. Tritium breeding ratios in the desired range can be obtained with blanket structures of modest thickness. A ferritic steel reflector behind the blanket aids in neutron reflection and shielding of the coil and retains a large fraction of the energy for use in the power cycle. The total thickness of the blanket and reflector is 0.65 m. An additional 0.3 m of iron shielding is used between the HF windings, and 0.23 m is used under the outboard part of the HF windings. The blanket and reflector are cooled in series with helium

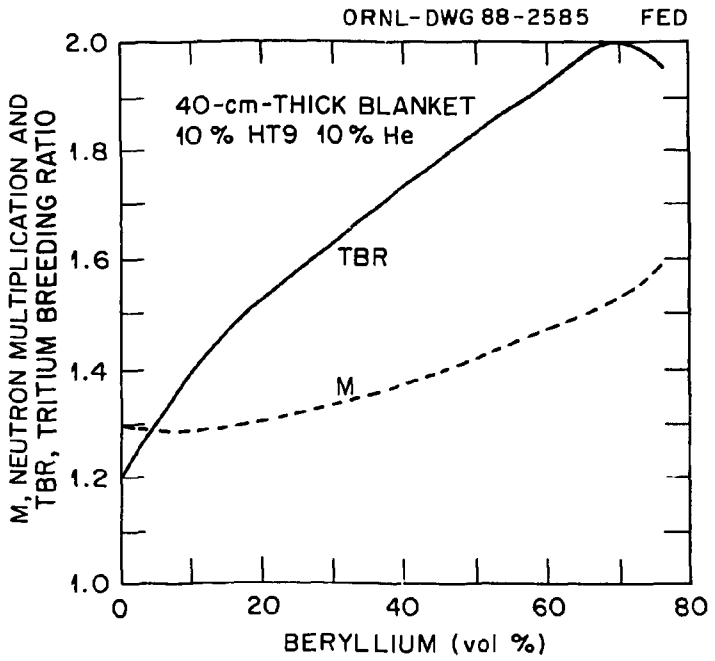

Fig. 5. Effect of beryllium volume fraction on tritium breeding ratio and neutron multiplication factor for a 40-cm-thick blanket.

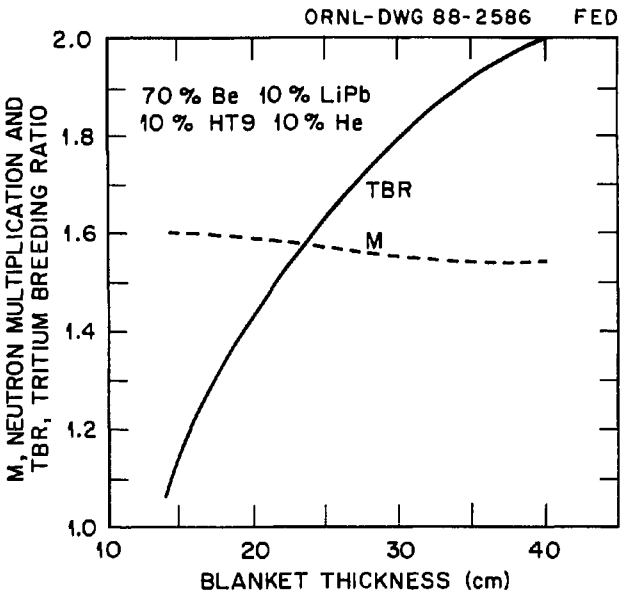

Fig. 6. Effect of blanket thickness on tritium breeding ratio and neutron multiplication factor for a blanket with 70% beryllium.

gas at 80 atm with an inlet temperature of 275°C and an outlet temperature of 575°C. This blanket would give a local energy multiplication of 1.55, an overall energy multiplication of 1.26, and a gross power cycle efficiency of 42.7%. Thus, this type of blanket is more than adequate to meet the tritium breeding requirements for the ATRs listed in Table IV.

VI. THE REACTOR CONFIGURATION

Figure 7 shows a top view of the torsatron winding without its shield for the ATR-2 configuration as well as the VF coil, the vacuum chamber, and coil supports. The helical coils are assumed to be made of Nb_3Sn ICCS wound as continuous coils in the coil case. Figure 8 shows a side view of the reactor configuration in a toroidal bell jar which serves as the vacuum chamber. The evacuated toroidal enclosure

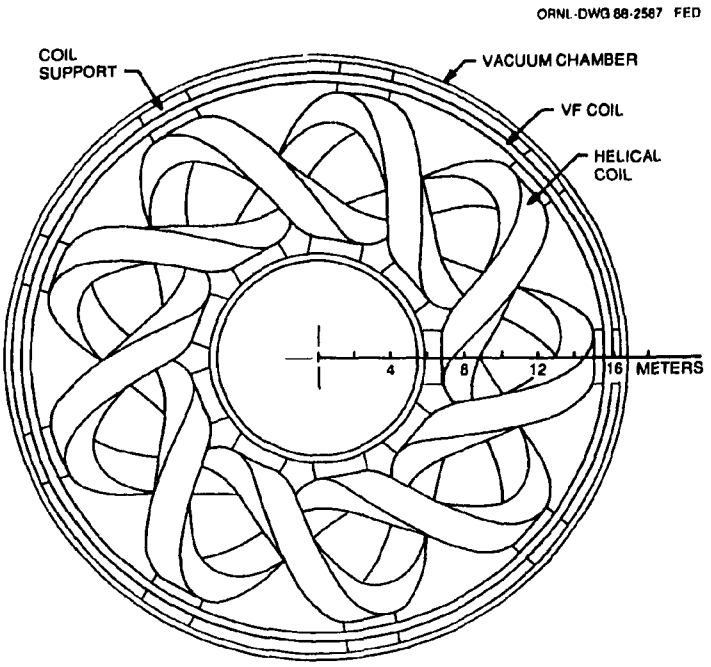

Fig. 7. Top view of an ATR-2 reactor. The HF windings shown enclose the conductor, coil case, and cryostat but not the neutron shielding.

has fixed vertical side walls and rotatable top and bottom lids with hatches. The helical coils, VF coils, shield, blanket, etc., are supported on the massive cylindrical side walls of the vacuum vessel. The coils are supported at the outer midplane perimeters by cold/warm struts that are flexible enough to allow for expansion and contraction due to heating and cooling. All service lines (electrical leads, coolant lines, etc.) penetrate the vacuum chamber through the side walls and are recessed out of the way for vertical extraction of the blanket modules. The coolant manifolds and the single pair of VF coils are also located where they will not interfere with blanket maintenance. In addition, ample space is available on the outboard side at other toroidal locations for a divertor-based impurity control system, as discussed in Sec. II.

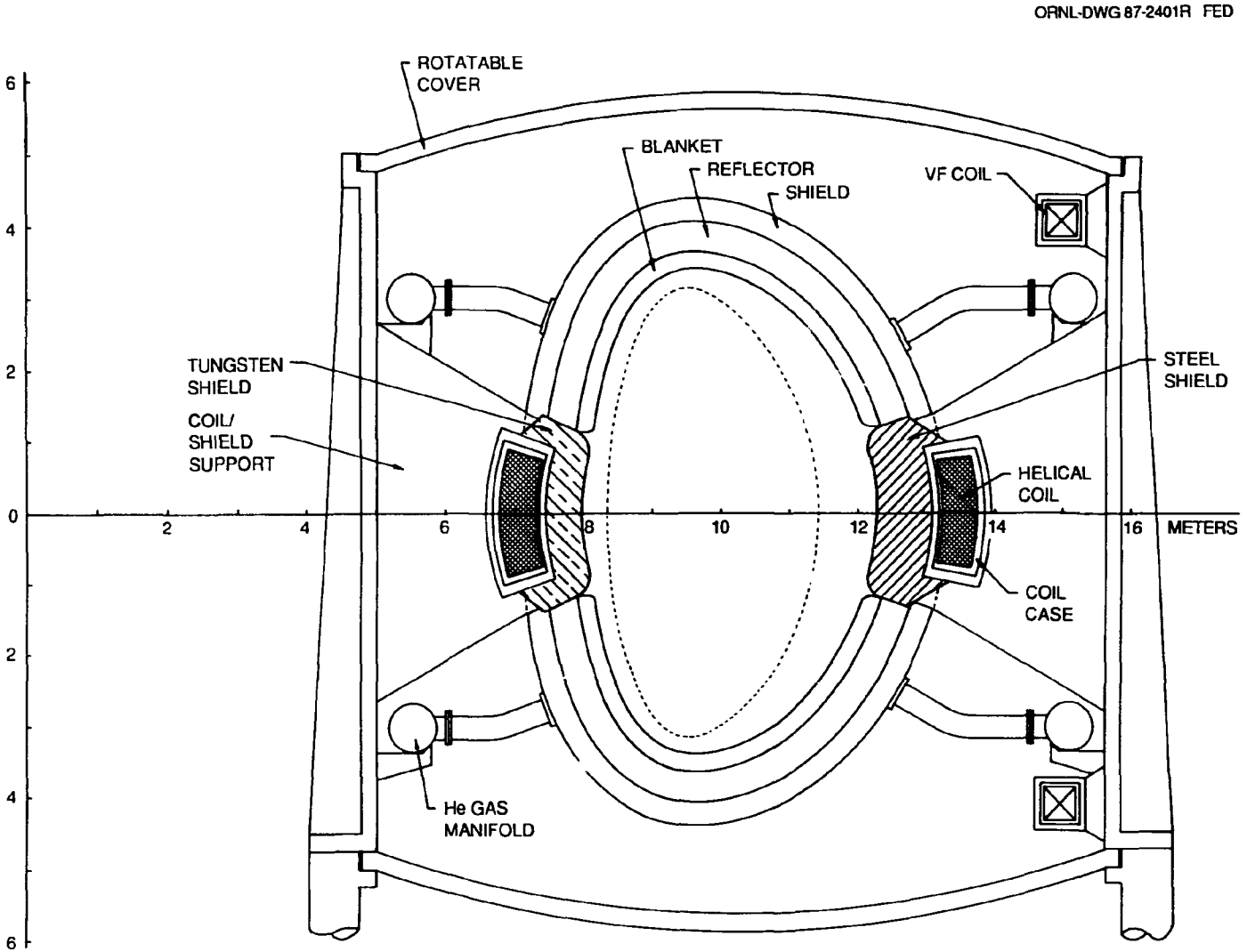

Fig. 8. Cross section of an ATR-2 reactor.

Reactor maintenance takes advantage of the good vertical access between the helical coils shown in Fig. 7. In normal operation, the upper and lower lids are sealed to the vertical sides of the chamber. During maintenance periods, the lids are unsealed and rotated about the reactor axis so that the access hatch indexes over (or below) the area to be maintained. The hatch is removed and remote maintenance machines disconnect service lines, etc. Overhead cranes then disconnect and remove blanket modules on the top side, and special elevated carriages do the same on the bottom side. This maintenance scheme is unique among fusion reactor designs proposed thus far and can only be applied to stellarator-like devices. Figure 8 shows the blanket segment cut at the point where the coils cross the horizontal midplane. The blanket segment actually extends farther down between the coils than is shown in the figure. During removal of a blanket segment, vertical motion has to be accompanied with a rotation in order to extract the segment from between the coils. This may be more evident from Fig. 7, which shows a top view of the HF coil set in the bell jar. The water-cooled plasma-side layer (first 15 cm) of the neutron shields must also be replaced periodically. Both the tungsten and steel neutron shields would incorporate boron carbide. The remainder of the shield is part of the coil structure.

VII. REACTOR PERFORMANCE

WHIST 1-D transport code calculations[20] have been performed for the $M = 6$, 9, and 12 cases for a variety of assumptions to study transport losses and their sensitivity to various parameters. The transport calculations sum the electric-field-dependent neoclassical value for ripple-induced losses formulated by Shaing[21] for the ions and electrons, the Hinton-Hazeltine value for axisymmetric neoclassical transport multiplied by 2 for the ions and 20 for the electrons, and twice the neo-Alcator anomalous transport value for the electrons. Fixed radial profiles for the

plasma density and electric field are assumed because of the large uncertainties in particle transport and the self-consistent radial electric field. However, the sensitivity to these profile assumptions is examined. The present calculations use an equivalent circular torus and $\epsilon_h(r)$ and $\iota(r)$ for the magnetic geometry. The actual magnetic geometry in flux coordinates is being incorporated into the $1\frac{1}{2}$-D version of WHIST.

Figure 9 shows the results for the $M = 9$ (ATR-2) case; contours of constant auxiliary power input, fusion power produced, and volume-averaged beta are plotted in an $\langle n \rangle$-$\langle T \rangle$ plane. Here $\langle n \rangle$ is the volume-averaged electron density and $\langle T \rangle$ is the density-averaged mean plasma temperature. This reference case assumes a

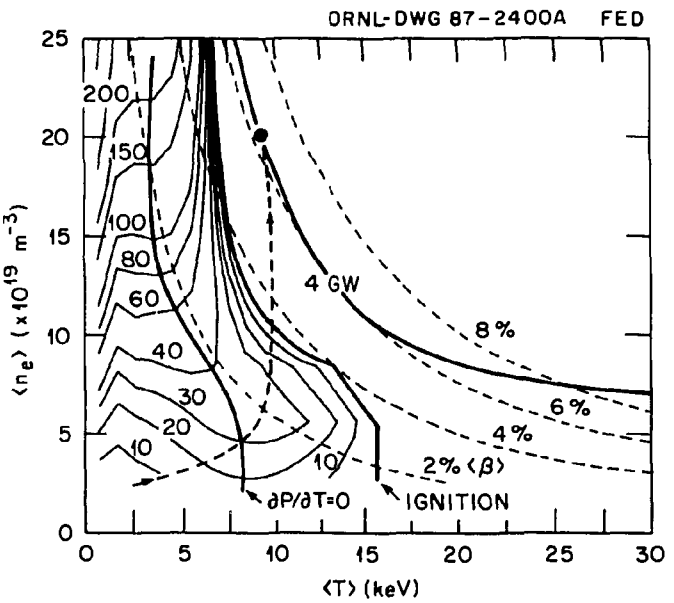

Fig. 9. WHIST transport code calculations for the ATR-2 reactor assuming a neoclassical confinement model and $\Phi_0 = 2\ T_i(0)$. Contours of constant auxiliary power input (light lines ranging from 10 to 200 MW) and volume-average beta (dashed lines ranging from 2 to 8%) are shown in the $\langle n \rangle$-$\langle T \rangle$ plane. The 4-GW fusion power production contour, the ignition contour (zero power input), and the line to the right of which the plasma is thermally unstable ($\partial P/\partial T < 0$) are indicated by heavier solid lines. The heavy dashed line with arrows indicates a path to a 4-GW, $\langle n_e \rangle = 2 \times 10^{20}$ m^{-3} operating point requiring $\simeq$34 MW of auxiliary heating power.

D-T plasma, $R_0 = 10.54$ m, $\bar{a} = 2.26$ m, $B_0 = 5$ T, Gaussian external power deposition profile $e^{-(r/b)^2}$ with $b = \bar{a}/2$ and a fraction $f_i = 0.7$ to the ions, a potential profile $\Phi = \Phi_0[1-(r/\bar{a})^p]$ with $p = 2$ and $\Phi_0 = 2\,T_i(0)$, and density profiles $n \propto [1-f(r/\bar{a})^2]^q$ with $f = 0.9$ and $q = 2$. The light lines indicate auxiliary heating powers ranging from 200 MW to 0 (the heavy ignition line), the dark lines indicate the thermal runaway contour (to the right of which $\partial P/\partial T < 0$) and the 4000-MW fusion power contour, and the dashed lines indicate contours of constant $\langle\beta\rangle$. A path to a 4-GW operating point at $\langle n_e\rangle = 2\times10^{20}$ m^{-3} requiring $\simeq$30 MW of auxiliary heating is indicated by the dotted curve. At the operating point shown, $T_i(0) = 10.4$ keV, $T_e(0) = 11.1$ keV, $\langle T\rangle = 9.4$ keV, $\langle\beta\rangle = 6.3\%$, and $n\tau = 3\times10^{20}$ m^{-3} s.

Table V gives the resulting plasma parameter values for ATR-1, ATR-2, and ATR-3. Compared to the reference $M = 9$ (ATR-2) case, the $M = 6$ (ATR-1) case requires slightly more power for ignition but achieves it at a higher value of temperature and beta, whereas the $M = 12$ (ATR-3) case requires slightly less power to reach ignition but again at a higher value of temperature and beta. The same trends hold for different operating points for ATR-1, ATR-2, and ATR-3.

Sensitivities to the parameters R_0, $\bar{a}$, B_0, b, f_i, $\Phi_0/T_i(0)$, p, f, and q have been studied in detail for the ATR-2 case. For the base case, ignition occurs at $\langle T\rangle = 10.1$ keV for $\langle n\rangle = 10^{20}$ m^{-3} and $\langle T\rangle = 7.1$ keV for $\langle n\rangle = 2\times10^{20}$ m^{-3}. The ignition margin is increased if the density profile is more peaked, the field is increased ($B_0 = 7$ T), the potential is increased [$\Phi_0/T_i(0) = 5$] or is broader ($p = 4$), the edge density is reduced ($f = 0.95$), or the reactor is larger (by 25% in R_0). Less margin for ignition occurs if the field is reduced ($B_0 = 3.5$ T), the edge density is increased ($f = 0.8$), Φ is linear in r ($p = 1$), or all the auxiliary power goes to the electrons ($f_i = 0$). Ignition does not occur, or occurs only at higher densities with higher auxiliary heating powers, if the potential is zero or the density

TABLE V.

Reactor Plasma Parameters

Parameter	ATR-1	ATR-2	ATR-3
R_0 (m)	8.37	10.54	11.13
$\bar{a}$ (m)	2.16	2.26	1.43
Volume (m^3)	770	1060	450
$\langle n_e \rangle$ (10^{20} m^{-3})	2	2	2
T_{i0} (keV)	11.9	10.4	14.4
T_{e0} (keV)	12.7	11.1	14.4
$\langle \beta \rangle$ (%)	7.2	6.3	9
P_{heating} (MW)	$\simeq$33	$\simeq$30	$\simeq$25
P_{fusion} (GW)	4	4	4
Γ_{neutron} (MW/m^2)	3.38	2.69	3.92

profile is broad ($q \lesssim 3/2$). There is little effect if the auxiliary heating profile shape changes ($b = \bar{a}$ or $\bar{a}/4$) or all the power goes to the ions ($f_i = 1$). Thus, there is a reasonable margin for ignition in low-aspect-ratio torsatron reactors at sizes one-half to one-third those of more conventional designs. More exact calculations must await experimental data from low-A_p torsatrons on electron energy losses at low collisionality.

VIII. D-T BURNERS

Reactors are, by their very nature, large devices since they must be economical, which implies superconducting coils and hence adequate distance for neutron shielding, which forces the large size. However, copper-coil ignition (or high-Q)

devices have very different constraints. The purpose of these devices is to study the behavior of a burning D-T plasma for a limited period and not to generate power for many years; hence, power-consuming copper coils can be used that do not require thick neutron shielding and thus permit a more compact and less expensive device. An example is the proposed Compact Ignition Tokamak[22] (CIT) that would study the physics of a burning tokamak plasma for short pulses ($\sim 10\tau_E$) prior to a more ambitious tokamak Engineering Test Reactor that would ignite and burn for a much longer pulse.

A successful D-T burning demonstration in a CIT would address many of the D-T physics issues relevant for a toroidal confinement approach. However, there may be issues that are concept specific that would require a stellarator D-T burner. Some of these issues are confinement of alpha particles, burn control, ash removal, and MHD equilibrium and stability, all of which depend on the details of the magnetic configuration.[23]

The optimum size for a copper-coil D-T burner is determined by considerations different from those for a reactor. Coil shielding, adequate space for tritium breeding, and maximum field on the conductor are no longer constraints. Instead, conductor heating, power required, cost, and the desired gap between HF windings on the small R side are the important constraints. Figure 10 shows for the $M = 9$ case the variation of the HF winding power $P_{\rm HF}$ and the HF winding mass $M_{\rm HF}$ (proportional to coil cost) versus R_0 for two limiting assumptions: (a) a maximum current density $j = 3$ kA/cm^2, $K \leq K_{\rm max}$; and (b) a maximum elongation $K = K_{\rm max}$, $j = j_{\rm min} \leq 3$ kA/cm^2. Here $K_{\rm max}$ is the value of K for which there is no longer any gap between HF windings on the small R side, and $j = j_{\rm min}$ is chosen so that all available radial depth is also used for the conductor. The other parameters assumed are $B_0 = 5$ T and $\Delta_0 = 0.25$ m for the total plasma-wall separation, first

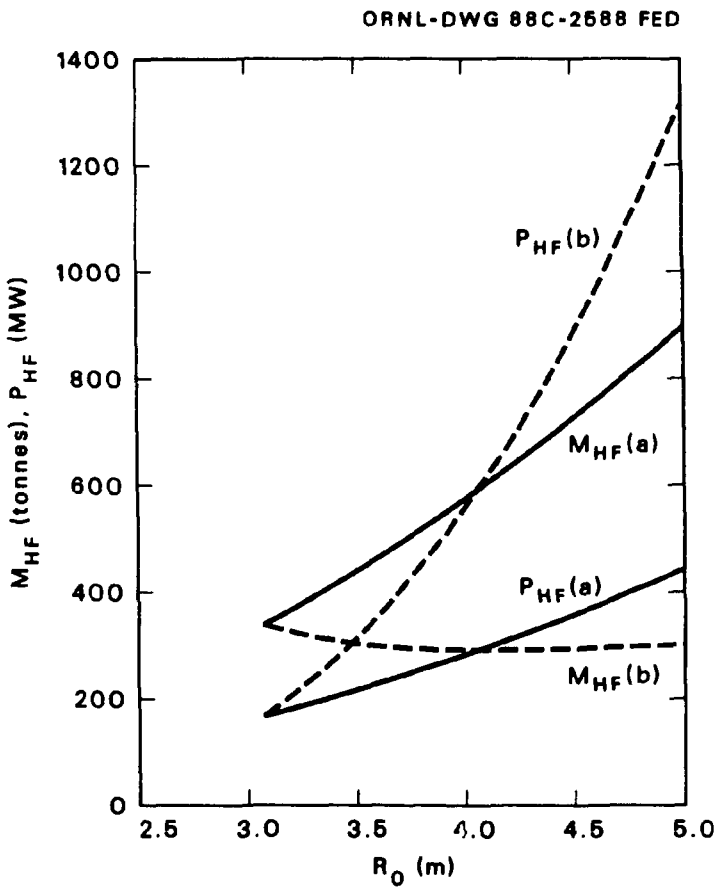

Fig. 10. Variation of power dissipation P_{HF} and coil volume V_{HF} (proportional to cost) for an $M = 6$ D-T burner for (a) $j_{\max} = 3$ kA/cm^2 (solid lines) and (b) $K = K_{\max}$ (dashed lines).

wall thickness, gap, and coil case thickness. The HF coil mass scales approximately as $B_0 R_0^2/(Mj)$ and the HF coil power as $B_0 R_0^2 j/M$.

Assumption (a), $j = 3$ kA/cm^2, corresponds to minimum capital cost but maximum operating (power) cost. Assumption (b), $K = K_{\max}$ and $j = j_{\min}$, corresponds to the converse. As R_0 increases, $j_{\min}$ and $K_{\max}$ decrease, as shown here for $M = 9$:

R_0 (m)	3.07, R_0 (min)	3.5	5.0
j_{min} (kA/cm^2)	3	2.07	1.01
K_{max}	6.40	4.88	3.18

The minimum R_0, $(R_0)_{min}$, increases weakly with M; $(R_0)_{min}$ is 2.58 m for $M = 6$, 3.07 m for $M = 9$, and 3.23 m for $M = 12$. The dependence of j_{min} and K_{max} on M for $R_0 = 4$ m is as follows:

M	6	9	12
j_{min} (kA/cm^2)	1.26	1.53	1.61
K_{max}	2.64	4.01	4.14

The largest component of the total device cost is that associated with the HF winding and its power supply. The total capital cost (including HF and VF coils, power supply, vacuum vessel, and assorted indirect costs) for these devices scales as $B_0^{0.84} R_0^{1.96} M^{-0.82}$. Increasing B_0 to 7 T reduces beta, improves confinement, and provides additional margin for ignition. In this case, the curves in Fig. 10 must be modified as follows: for assumption (a), $P_{HF} \rightarrow 1.4 P_{HF}$ and $M_{HF} \rightarrow 0.71 M_{HF}$; for assumption (b), $P_{HF} \rightarrow 1.96 P_{HF}$ and M_{HF} is unchanged. For fixed current density, the capital cost would increase by 33%. Since power (and power supply cost) is proportional to j and coil cost is proportional to $1/j$, the total capital cost could be reduced by going to even higher j at the penalty of shorter pulse length and higher operating costs. Conversely, the very large ohmic power requirement can be minimized at the penalty of higher capital cost in the extreme case where all the available space is used for the coil cross section [assumption (b)]. However, operating cost is the lesser issue since the average power required is a small fraction of the peak power because of the low duty cycle; hence, assumption (a) is more appropriate.

A disadvantage of copper coils is the high peak power required. The power requirements and pulse length limitations for a copper-coil D-T burner depend on the specific coil parameters chosen. Here we assume a conservative value of $j_{ss} = 3$ kA/cm^2 for steady-state water-cooled copper coils. For $j > j_{ss}$, water cooling is not effective during the pulse but is adequate to restore the coil temperature between pulses. The uncooled pulse length is $\Delta t_{UC} = 1.68\Delta T/j^2$, where the temperature rise ΔT is in degrees Celsius. This time is not long enough to study long-pulse issues with D-T plasmas. For $\Delta T = 100°C, \Delta t_{UC} = 18.7$ s for $j = 3$ kA/cm^2 and 6.7 s for $j = 5$ kA/cm^2. Water cooling increases the pulse length by a factor $j^2/(j^2 - j_{ss}^2)$. The improvement is marginal because this factor is only 2.78 for $j = 1.25j_{ss}$, 1.8 for $j = 1.5j_{ss}$, and 1.33 for $j = 2j_{ss}$. Substantial improvements in j_{ss} beyond 3 kA /cm^2 would require large increases in the fractional area assumed for water cooling (0.18) and in the flow velocity (6 m/s) and a large decrease in the length of the cooling path (one turn assumed), but j_{ss} depends only weakly (square root) on these quantities.

We consider three D-T burner cases (ATB-1, ATB-2, and ATB-3 with $M = 6$, 9, and 12) that correspond to the ATR reactor cases considered earlier. A major radius of 4 m was chosen. These devices have unshielded copper coils, whereas larger D-T burners such as Heliotron F2 (Ref. 24) with $R_0 = 8$ m, ASB06E (Ref. 25) with $R_0 = 15.2$ m, and TNPP (Ref. 8) with $R_0 = 36$ m have superconducting coils and shielding. Table VI lists the HF coil parameters for the three ATB cases.

Monte Carlo calculations of alpha particle confinement for this geometry[16] indicate that $\simeq$30% of the alphas are lost from the plasma. These loss fractions are acceptable for a first test of the effects of alpha-particle heating on stellarator behavior. The heating power required to attain the plasma parameters sufficient to produce $Q \gtrsim 10$ depends on the value of the bulk heat diffusivity χ_i [$\lesssim 1$ m^2·s^{-1}

TABLE VI.

HF Coil Parameters for D-T Burners

Parameter	ATB-1	ATB-2	ATB-3
M	6	9	12
R_0 (m)	4	4	4
r_0 (m)	1.6	1.23	0.89
Radial depth (m)	0.71	0.43	0.34
I_{HF} (MA·turns)	16.7	11.1	8.33
B_0 (T)	5	5	5
Assumption (a), $j = 3$ kA/cm^2, $K \leq K_{max}$			
Volume (m^3)	43.6	31.9	23.3
Power (MW)	785	574	420
Assumption (b), $j \leq 3$ kA/cm^2, $K = K_{max}$			
Volume (m^3)	104	62.5	43.6
Power (MW)	330	292	224

obtained in various transport calculations[26] assuming $\Phi_0/T_i(0) \sim 2$–3], the plasma size, and the value of the confining magnetic field. Figure 11 shows the WHIST transport code calculations for the ATB-2 case using the same assumptions used in Fig. 9 (ATR-2). The zero auxiliary heating power contour in Fig. 11 indicates ignition, so relatively high values of Q seem achievable in this device. The parameters corresponding to points A ($Q = 10$) and B ($Q = \infty$) in Fig. 11 are given in Table VII. In this case point A is thermally unstable and the plasma would move to point B unless additional losses are introduced.

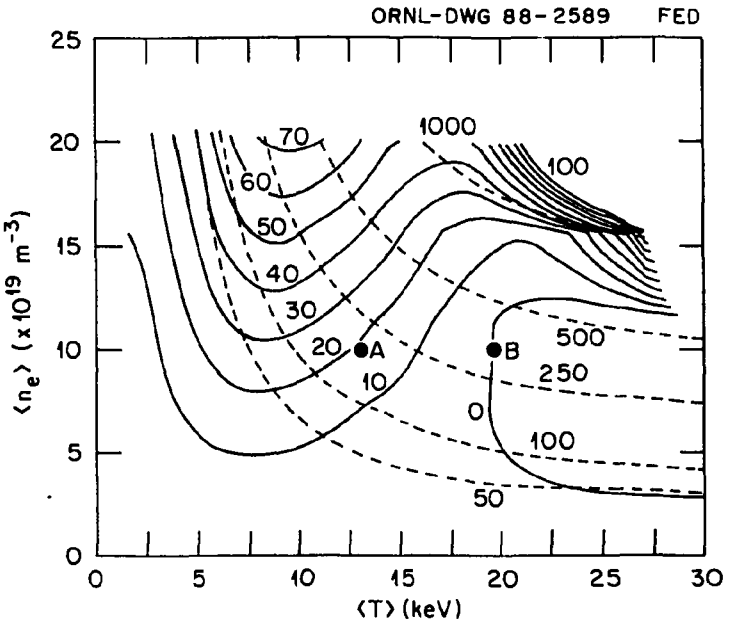

Fig. 11. WHIST transport code calculations for an $M = 9$ D-T burner similar to the ATR-2 reactor case shown in Fig. 9. Solid lines (0 to 200 MW): contours of constant auxiliary heating; dashed lines (50 to 1000 MW): contours of constant fusion power. The contours are distorted in the upper right-hand corner by a beta limit introduced via a rapid enhancement of χ_e and χ_i at $\langle\beta\rangle \sim 20\%$.

IX. CONCLUSIONS

Low-aspect-ratio torsatrons are good candidates for compact reactors and D-T burner experiments. The three cases examined in this study illustrate the feasibility of these reactor configurations. Both compact torsatron reactors with $R_0 = 8$–11 m and D-T burners with $R_0 \simeq 4$ m are practical for $M = 6$, 9, and 12. The values obtained for $\langle\beta\rangle$ and Γ_n are not high. Neoclassical electron ripple transport allows ignition for relatively low values of auxiliary input power if adequate shaping of the plasma density near the edge is possible (as in the tokamak H-mode). A new and attractive maintenance scheme has been developed for these devices. A tritium breeding blanket with a high beryllium fraction can provide the required

TABLE VII.

Plasma Parameters for D-T Burners

Parameter	ATB-1	ATB-2	ATB-3
R_0 (m)	4	4	4
$\bar{a}$ (m)	1.03	0.86	0.51
Volume (m^3)	84.4	58.2	20.9
$\langle n_e \rangle$ (10^{20} m^{-3})	1	1	1
$Q = 10$			
T_{i0} (keV)	16.3	16.0	15.2
T_{e0} (keV)	12.0	11.8	11.2
$\langle \beta \rangle$ (%)	4.78	4.65	4.45
P_{heating} (MW)	27.6	18.7	6.5
P_{fusion} (MW)	270	192	61
Γ_{neutron} (MW/m^2)	0.95	0.79	0.78
$Q = \infty$			
T_{i0} (keV)	25.2	24.1	22.2
T_{e0} (kev)	18.0	17.5	16.8
$\langle \beta \rangle$ (%)	8.0	7.65	7.15
P_{heating} (MW)	38.3	28.0	11.3
P_{fusion} (MW)	490	339	107
Γ_{neutron} (MW/m^2)	1.72	1.40	0.66

breeding ratio without breeding under the inboard half of the HF windings. The minimum-size reactors studied are relatively insensitive to assumptions on the HF winding parameters. All three cases look attractive and have some margin to relax some of the constraints assumed. The most serious issue for compact torsatrons, and indeed any stellarator, is the unknown scaling of plasma confinement with aspect ratio, temperature (or collisionality), and beta. Some of this information will be obtained from new stellarator experiments nearing operation, but much of the needed information will have to await the next generation of large stellarators now under design, and beyond.

ACKNOWLEDGMENTS

The authors acknowledge useful discussions with R. A. Dory, W. A. Houlberg, M. S. Lubell, S. L. Painter, and J. Sheffield and the encouragement of O. B. Morgan and M. W. Rosenthal of Oak Ridge National Laboratory. This research was sponsored by the Office of Fusion Energy, U.S. Department of Energy, under contract DE-AC05-84OR21400 with Martin Marietta Energy Systems, Inc.

REFERENCES

1. J. SHEFFIELD, "Physics Requirements for an Attractive Magnetic Fusion Reactor," *Nucl. Fusion*, **25**, 1733 (1985).

2. F. WAGNER, O. GRUBER, K. LACKNER, H. D. MURMANN, E. SPETH, et al., "Experimental Study of the Principles Governing Tokamak Transport," *Phys. Rev. Lett.*, **56**, 2187 (1986).

3. J. F. LYON, B. A. CARRERAS, J. H. HARRIS, J. A. ROME, et al., "Stellarator Physics Evaluation Studies," *Proc. 9th Int. Conf. Plasma Physics and Controlled Nuclear Fusion Research*, Baltimore, Maryland, 1982, Vol. 3, p. 115, International Atomic Energy Agency, Vienna (1983).

4. L. GARCIA, B. A. CARRERAS, J. H. HARRIS, H. R. HICKS, and V. E. LYNCH, "Equilibrium Studies for Low-Aspect-Ratio Torsatrons," *Nucl. Fusion*, **24**, 115 (1984).

5. J. F. LYON, B. A. CARRERAS, K. K. CHIPLEY, M. J. COLE, J. H. HARRIS, et al., "The Advanced Toroidal Facility," *Fusion Technol.*, **10**, 179 (1986).

6. T. MATSUI, H. NAKASHIMA, et al., "Nuclear Design of a Heliotron-H Fusion Power Reactor," *J. Fusion Energy*, **4**, 45 (1985).

7. G. GRIEGER, E. HARMEYER, et al., "Advanced Stellarator Reactor and Burner Studies," *Proc. 4th Technical Committee Meeting and Workshop on Fusion Reactor Design and Technology*, Yalta, U.S.S.R., 1986, International Atomic Energy Agency, Vienna (to be published).

8. V. V. ANISIMOV, I. M. ARTYUGINA, et al., "Choice of Parameters and Techno-Economical Estimates for a Thermonuclear Power Plant with Pure Torsatron Reactor," *Problems of Atomic Science and Technology*, Vol. 2, p. 16 (1984).

9. B. A. CARRERAS, H. R. HICKS, J. A. HOLMES, V. E. LYNCH, et al., "Equilibrium and Stability Properties of High-Beta Torsatrons," *Phys. Fluids*, **26**, 3569 (1983).

10. B. A. CARRERAS, N. DOMINGUEZ, L. GARCIA, V. E. LYNCH, J. F. LYON, et al., "Compact Torsatron Configurations," submitted to *Nucl. Fusion*; see also ORNL/TM-10030, Oak Ridge National Laboratory (1987).

11. B. A. CARRERAS, J. F. LYON, V. E. LYNCH, and S. L. PAINTER, "Scaling Properties of Compact Torsatrons" (unpublished, 1988).

12. J. T. LACATSKI, W. A. HOULBERG, and N. A. UCKAN, "Plasma Engineering Analysis of a Small Torsatron Reactor," ORNL/TM-9533, Oak Ridge National Laboratory (1985).

13. W. N. G. HITCHON, "Reduced-Aspect-Ratio Stellarator Reactors," *Nucl. Fusion*, **24**, 91 (1984).

14. E. D. VOLKOV, A. V. GEORGIEZSKIJ, Yu. K. KUZNETSOV, Yu. A. LITVINENKO, O. S. PAVLICHENKO, V. A. RUDAKOV, and Yu. SERGEEV, "Fundamental Concepts of a Reactor-Torsatron with an Additional Longitudinal Field" (unpublished), Institute of Physics and Technology, Ukrainian Academy of Sciences, Kharkov 310108, U.S.S.R.

15. R. H. FOWLER, J. A. ROME, and J. F. LYON, "Monte-Carlo Studies of Transport in Stellarators," *Phys. Fluids*, **28**, 338 (1985).

16. S. L. PAINTER, Oak Ridge National Laboratory, private communication, 1987.

17. M. E. SAWAN, University of Wisconsin–Madison, private communication, 1987.

18. P. L. WALSTROM, "Stability Limit Guidelines for Superconducting Coil Design," UWFDM-611, University of Wisconsin (March 1985).

19. I. N. SVIATOSLAVSKY, M. E. SAWAN, L. A. EL-GUEBALY, L. J. WITTENBERG, and M. L. CORRADINI, "Thin Blanket Design for MINIMARS — A Compact Tandem Mirror Fusion Reactor," *Fusion Technol.*, **10**, 609 (1986).

20. W. A. HOULBERG, S. E. ATTENBERGER, and L. M. HIVELY, "Contour Analysis of Fusion Reactor Plasma Performance," *Nucl. Fusion*, **22**, 935 (1982).

21. K. C. SHAING, "Stability of the Radial Electric Field in a Nonaxisymmetric Torus," *Phys. Fluids*, **27**, 1567 (1984).

22. J. SCHMIDT, G. BATEMAN, D. BLACKFIELD, L. BROMBERG, C. BUSHNELL, et al., "A Compact Ignition Experiment," *Proc. 11th Int. Conf. Plasma Physics and Controlled Nuclear Fusion Research*, Kyoto, Japan, 1986, International Atomic Energy Agency, Vienna (in press, 1987) paper IAEA-CN-47/H-I-2.

23. Magnetic Fusion Advisory Committee, "Report on Assessment of Burning-Plasma Phenomena in a Compact Ignition Tokamak Presented to the Magnetic Fusion Advisory Committee by Panel XIV" (unpublished), February 10, 1986.

24. Y. KAZAWA, Y. ITOU, S. SUZUKI, T. OKAZAKI, O. MOTOJIMA, and K. UO, "Conceptual Design Study of Heliotron Reactors (F2, I)," p. 540 in *Proc. Int. Stellarator/Heliotron Workshop*, Kyoto, Japan, PPLK-6, Kyoto University (1986).

25. E. HARMEYER, J. KISSLINGER, F. RAU, and H. WOBIG, "Some Aspects of Modular Stellarator Reactors," *Proc. 10th Int. Conf. Plasma Physics and Controlled Nuclear Fusion Research*, London, 1984, Vol. III, p. 363, International Atomic Energy Agency, Vienna (1985).

26. E. C. CRUME, Jr., K. C. SHAING, S. P. HIRSHMAN, and W. I. VAN RIJ, "Transport Scaling in the Collisionless-Detrapping Regime of Stellarators." *Phys. Fluids*, **31**. 11 (1988): see also ORNL TM-10574. Oak Ridge National Laboratory (1987).

ORNL/TM-10572
Dist. Category UC-421, 424, 426, 427

INTERNAL DISTRIBUTION

1. L. A. Berry
2–11. B. A. Carreras
12. R. A. Dory
13. J. L. Dunlap
14. R. H. Fowler
15. J. H. Harris
16. H. H. Haselton
17. P. N. Haubenreich
18. S. P. Hirshman
19. R. C. Isler
20. M. S. Lubell
21. V. E. Lynch
22–31. J. F. Lyon
32. P. K. Mioduszewski
33. O. B. Morgan
34. M. Murakami
35. G. H. Neilson
36. Y-K. M. Peng
37. J. A. Rome
38. M. W. Rosenthal
39. M. J. Saltmarsh
40. T. E. Shannon
41. J. Sheffield
42. P. B. Thompson
43. J. S. Tolliver
44–45. Laboratory Records Department
46. Laboratory Records, ORNL-RC
47. Document Reference Section
48. Central Research Library
49. Fusion Energy Division Library
50–51. Fusion Energy Division Publications Office
52. ORNL Patent Office

EXTERNAL DISTRIBUTION

53. Office of the Assistant Manager for Energy Research and Development, U.S. Department of Energy, Oak Ridge Operations Office, P. O. Box E, Oak Ridge, TN 37831
54. J. D. Callen, Department of Nuclear Engineering, University of Wisconsin, Madison, WI 53706-1687
55. J. F. Clarke, Director, Office of Fusion Energy, Office of Energy Research, ER-50 Germantown, U.S. Department of Energy, Washington, DC 20545
56. R. W. Conn, Department of Chemical, Nuclear, and Thermal Engineering, University of California, Los Angeles, CA 90024
57. S. O. Dean, Fusion Power Associates, 2 Professional Drive, Suite 248, Gaithersburg, MD 20879
58. H. K. Forsen, Bechtel Group, Inc., Research Engineering, P. O. Box 3965, San Francisco, CA 94105
59. J. R. Gilleland, Lawrence Livermore National Laboratory, P.O. Box 5511, Livermore, CA 94550

60. R. W. Gould, Department of Applied Physics, California Institute of Technology, Pasadena, CA 91125
61. R. A. Gross, Plasma Research Laboratory, Columbia University, New York, NY 10027
62. D. M. Meade, Princeton Plasma Physics Laboratory, P.O. Box 451, Princeton, NJ 08544
63. M. Roberts, International Programs, Office of Fusion Energy, Office of Energy Research, ER-52 Germantown, U.S. Department of Energy, Washington, DC 20545
64. W. M. Stacey, School of Nuclear Engineering and Health Physics, Georgia Institute of Technology, Atlanta, GA 30332
65. D. Steiner, Nuclear Engineering Department, NES Building, Tibbetts Avenue, Rensselaer Polytechnic Institute, Troy, NY 12181
66. R. Varma, Physical Research Laboratory, Navrangpura, Ahmedabad 380009, India
67. Bibliothek, Max-Planck-Institut für Plasmaphysik, D-8046 Garching, Federal Republic of Germany
68. Bibliothek, Institut für Plasmaphysik, KFA, Postfach 1913, D-5170 Julich, Federal Republic of Germany
69. Bibliotheque, Centre de Recherches en Physique de Plasmas, 21 Avenue des Bains, 1007 Lausanne, Switzerland
70. F. Prevot, CEN/Cadarache, Departement de Recherches sur la Fusion Controlee, F-13108 Saint-Paul-lez-Durance, France
71. Bibliotheque, CEN/Cadarache, Departement de Recherches sur la Fusion Controlee, F-13108 Saint-Paul-lez-Durance, France
72. Library, Culham Laboratory, UKAEA, Abingdon, Oxfordshire, OX14 3DB, England
73. Library, FOM-Instituut voor Plasmafysica, Rijnhuizen, Edisonbaan 14, 3439 MN Nieuwegein, The Netherlands
74. Library, Institute of Plasma Physics, Nagoya University, Nagoya 464, Japan
75. Library, International Centre for Theoretical Physics, P.O. Box 586, I-34100 Trieste, Italy
76. Library, Laboratorio Gas Ionizatti, CP 56, I-00044 Frascati, Rome, Italy
77. Library, Plasma Physics Laboratory, Kyoto University, 611 Gokasho, Uji, Kyoto, Japan
78. Plasma Research Laboratory, Australian National University, P.O. Box 4, Canberra, A.C.T. 2000, Australia
79. Thermonuclear Library, Japan Atomic Energy Research Institute, Tokai Establishment, Tokai-mura, Naka-gun, Ibaraki-ken, Japan
80. G. A. Eliseev, I. V. Kurchatov Institute of Atomic Energy, P. O. Box 3402, 123182 Moscow, U.S.S.R.
81. V. A. Glukhikh, Scientific-Research Institute of Electro-Physical Apparatus, 188631 Leningrad, U.S.S.R.

82. I. Shpigel, Institute of General Physics, U.S.S.R. Academy of Sciences, Ulitsa Vavilova 38, Moscow, U.S.S.R.
83. D. D. Ryutov, Institute of Nuclear Physics, Siberian Branch of the Academy of Sciences of the U.S.S.R., Sovetskaya St. 5, 630090 Novosibirsk, U.S.S.R.
84. V. T. Tolok, Kharkov Physical-Technical Institute, Academical St. 1, 310108 Kharkov, U.S.S.R.
85. Library, Academia Sinica, P.O. Box 3908, Beijing, China (PRC)
86. R. A. Blanken, Experimental Plasma Research Branch, Division of Applied Plasma Physics, Office of Fusion Energy, Office of Energy Research, ER-542, Germantown, U.S. Department of Energy, Washington, DC 20545
87. K. Bol, Princeton Plasma Physics Laboratory, P.O. Box 451, Princeton, NJ 08544
88. R. A. E. Bolton, IREQ Hydro-Quebec Research Institute, 1800 Montee Ste.-Julie, Varennes, P.Q. JOL 2P0, Canada
89. D. H. Crandall, Experimental Plasma Research Branch, Division of Applied Plasma Physics, Office of Fusion Energy, Office of Energy Research, ER-542 Germantown, U.S. Department of Energy, Washington, DC 20545
90. R. L. Freeman, GA Technologies, Inc., P.O. Box 81608, San Diego, CA 92138
91. K. W. Gentle, RLM 11.222, Institute for Fusion Studies, University of Texas, Austin, TX 78712
92. R. J. Goldston, Princeton Plasma Physics Laboratory, P.O. Box 451, Princeton, NJ 08544
93. J. C. Hosea, Princeton Plasma Physics Laboratory, P.O. Box 451, Princeton, NJ 08544
94. S. W. Luke, Division of Confinement Systems, Office of Fusion Energy, Office of Energy Research, ER-55 Germantown, U.S. Department of Energy, Washington, DC 20545
95. E. Oktay, Division of Confinement Systems, Office of Fusion Energy, Office of Energy Research, ER-55 Germantown, U.S. Department of Energy, Washington, DC 20545
96. D. Overskei, GA Technologies, Inc., P.O. Box 81608, San Diego, CA 92138
97. R. R. Parker, Plasma Fusion Center, NW 16-288, Massachusetts Institute of Technology, Cambridge, MA 02139
98. W. L. Sadowski, Fusion Theory and Computer Services Branch, Division of Applied Plasma Physics, Office of Fusion Energy, Office of Energy Research, ER-541 Germantown, U.S. Department of Energy, Washington, DC 20545
99. J. W. Willis, Division of Confinement Systems, Office of Fusion Energy, Office of Energy Research, ER-55 Germantown, U.S. Department of Energy, Washington, DC 20545
100. A. P. Navarro, Division de Fusion, Asociacion EURATOM/CIEMAT, Avenida Complutense 22, E-28040 Madrid, Spain
101. Laboratory for Plasma and Fusion Studies, Department of Nuclear Engineering, Seoul National University, Shinrim-dong, Gwanak-ku, Seoul 151, Korea

102. J. L. Johnson, Plasma Physics Laboratory, Princeton University, P.O. Box 451, Princeton, NJ 08544
103. L. M. Kovrizhnykh, Institute of General Physics, U.S.S.R. Academy of Sciences, Ulitsa Vavilova 38, 117924 Moscow, U.S.S.R.
104. O. Motojima, Plasma Physics Laboratory, Kyoto University, 611 Gokasho, Uji, Kyoto, Japan
105. V. D. Shafranov, I. V. Kurchatov Institute of Atomic Energy, P.O. Box 3402, 123182 Moscow, U.S.S.R.
106. J. L. Shohet, Torsatron/Stellarator Laboratory, University of Wisconsin, Madison, WI 53706
107. H. Wobig, Max-Planck Institut fur Plasmaphysik, D-8046 Garching, Federal Republic of Germany
108. N. A. Davies, Office of Fusion Energy, Office of Energy Research, ER-51 Germantown, U.S. Department of Energy, Washington, DC 20545
109. W. F. Dove, Office of Fusion Energy, Office of Energy Research, ER-543 Germantown, U.S. Department of Energy, Washington, DC 20545
110. R. J. Dowling, Office of Fusion Energy, Office of Energy Research, ER-53 Germantown, U.S. Department of Energy, Washington, DC 20545
111. D. Markevitch, Office of Fusion Energy, Office of Energy Research, ER-55 Germantown, U.S. Department of Energy, Washington, DC 20545
112. D. B. Nelson, Office of Fusion Energy, Office of Energy Research, ER-54 Germantown, U.S. Department of Energy, Washington, DC 20545
113. T. K. Chu, Plasma Physics Laboratory, Princeton University, P.O. Box 451, Princeton, NJ 08544
114. H. Furth, Plasma Physics Laboratory, Princeton University, P.O. Box 451, Princeton, NJ 08544
115. P. Rutherford, Plasma Physics Laboratory, Princeton University, P.O. Box 451, Princeton, NJ 08544
116. W. Stodiek, Plasma Physics Laboratory, Princeton University, P.O. Box 451, Princeton, NJ 08544
117. G. Grieger, Max-Planck-Institut für Plasmaphysik, D-8046 Garching bei München, Federal Republic of Germany
118. F. Rau, Max-Planck-Institut für Plasmaphysik, D-8046 Garching bei München, Federal Republic of Germany
119. H. Renner, Max-Planck-Institut für Plasmaphysik, D-8046 Garching bei München, Federal Republic of Germany
120. A. Iiyoshi, Plasma Physics Laboratory, Kyoto University, 611 Gokasho, Uji, Kyoto, Japan
121. K. Uo, Plasma Physics Laboratory, Kyoto University, 611 Gokasho, Uji, Kyoto, Japan
122. M. Wakatani, Plasma Physics Laboratory, Kyoto University, 611 Gokasho, Uji, Kyoto, Japan

123. M. Fujiwara, Institute of Plasma Physics, Nagoya University, Nagoya 464, Japan
124. H. Ikegami, Institute of Plasma Physics, Nagoya University, Nagoya 464, Japan
125. T. Uchida, Institute of Plasma Physics, Nagoya University, Nagoya 464, Japan
126. O. Pavlichenko, Kharkov Physico-Technical Institute, 310108 Kharkov, U.S.S.R.
127. R. Davidson, Plasma Fusion Center, Massachusetts Institute of Technology, NW16-202, 167 Albany St., Cambridge, MA 02139
128. I. N. Sviatoslavsky, Fusion Technology Institute, 529 Engineering Research Building, University of Wisconsin, 1500 Johnson Drive, Madison, WI 53706-1687
129. D. T. Anderson, Torsatron/Stellarator Laboratory, 1420 Engineering Building, 1415 Johnson Drive, Madison, WI 53706
130. H. Weitzner, Courant University of Mathematical Sciences, New York University, 251 Mercer Street, New York, NY 10012
131. P. R. Garabedian, Courant University of Mathematical Sciences, New York University, 251 Mercer Street, New York, NY 10012
132. K. B. Kartashev, I. V. Kurchatov Institute of Atomic Energy, P.O. Box 3402, 123182 Moscow, U.S.S.R.
133. G. H. Miley, 216 Nuclear Engineering Laboratory, University of Illinois, 103 S. Goodwin Avenue, Urbana, IL 61801
134. D. G. Swanson, Department of Physics, Auburn University, College Street, Auburn, AL 36849
135. F. L. Ribe, 319 Benson Hall, BF 10, University of Washington, 1400 Northwest Campus Parkway, Seattle, WA 98195
136. R. K. Linford, Controlled Thermonuclear Research Division, Los Alamos National Laboratory, P.O. Box 1663, Los Alamos, NM 87545
137. T. K. Fowler, L-640, Lawrence Livermore National Laboratory, P.O. Box 5511, Livermore, CA 94550
138. D. E. Baldwin, L-640, Lawrence Livermore National Laboratory, P.O. Box 5511, Livermore, CA 94550
139. A. J. Wootton, Fusion Research Center, RLM 11.222, The University of Texas at Austin, Austin, TX 78712
140. H. L. Berk, Institute for Fusion Studies, RLM 11.222, The University of Texas at Austin, Austin, TX 78712
141. T. Ohkawa, Fusion and Advanced Technologies, GA Technologies, Inc., P.O. Box 85608, San Diego, CA 92138
142. S. M. Hamberger, Plasma Research Laboratory, Research School of Physical Sciences, Australian National University, P.O. Box 4, Canberra, A.C.T. 2600, Australia

143. A. H. Boozer, Physics Department, College of William and Mary, Williamsburg, VA 23185
144. Library, JET Joint Undertaking, Abingdon, Oxon OX14 3EA, England
145. Library, Japan Atomic Energy Research Institute, Naka, Japan
146. Bibliothek, Kernforschungszentrum Karlsruhe GmbH, Postfach 3640, D-7500 Karlsruhe 1, Federal Republic of Germany
147. T. C. Hender, Culham Laboratory, UKAEA, Abingdon, Oxfordshire, OX14 3DB, England
148. A. Grau Malonda, Division de Fusion, Asociacion EURATOM/CIEMAT, Avenida Complutense 22, E-28040 Madrid, Spain

149-208. Given distribution as shown in TIC 4500, Magnetic Fusion Energy (Distribution Category UC-421, 424, 426, 427: Plasma Systems, Fusion Systems, Experimental Plasma Physics, Theoretical Plasma Physics)